Accounting for grain crushing and pore collapse for strain localization in rocks

N.A. Collins-Craft[1], J. Sulem[1], I. Stefanou[2], and I. Einav[3]

[1]Laboratoire Navier, École Nationale des Ponts et Chaussées, Institut Polytechnique de Paris, Université Gustave Eiffel, CNRS, Champs-sur-Marne, France
[2]IMSIA (UMR 9219), CNRS, EDF, ENSTA Paris, Institut Polytechnique de Paris, Palaiseau, France
[3]Particles and Grains Laboratory, The School of Civil Engineering, The University of Sydney, Sydney, Australia

15/05/2026

Abstract

We present a model for crushable granular rocks by embedding breakage mechanics in the Cosserat continuum. This model features a dependence on an enriched set of state variables (the elastic strains and curvatures, the density, the solid fraction, and the breakage state variable), demonstrates a dependence of the yield surface on the Lode angle, breakage and solid fraction, and evolution laws that tightly couple the competing processes. We then outline the notion of linear stability analysis and how we use this technique to obtain both the thickness and orientation of any shear bands that may form in the system. The model is then calibrated from data available in the literature on Fontainebleau sandstone and other similar granular rocks. We compare the model predictions with experimental measures of both the stress-strain response, and the width and angle of shear bands, and find good agreement with the results that have been previously reported.
Keywords: Grain crushing · Pore collapse · Cosserat continuum.

1 Introduction

The formation of shear and compaction bands is a typical failure mode for geomaterials, in both the laboratory and the field. Typical rate-independent continuum mechanics models are not able to predict finite thicknesses for shear bands due to the absence of an internal length scale [1]. The Cosserat continuum, which features an internal length scale, allows the prediction of finite thickness shear bands. However, in cases where the underlying grains crush, as is typically the case for granular rocks such as Fontainebleau sandstone, the internal length scale which is attached to the underlying grain size distribution (GSD) should also evolve. We thus present a model drawn from the breakage mechanics family [2, 3] embedded in the Cosserat continuum framework [4] that accounts for grain size evolution and porosity change [5] while being able to predict finite shear band width.

2 Theoretical development

2.1 Definitions

We introduce the breakage state variable B given by

$$B = \frac{\int_{d_{min}}^{d_{Max}} [\hat{p}(w) - \hat{p}_0(w)] \mathrm{d}w}{\int_{d_{min}}^{d_{Max}} [\hat{p}_u(w) - \hat{p}_0(w)] \mathrm{d}w}, \tag{1}$$

where $\hat{p}_0, \hat{p}, \hat{p}_u$ are the probability densities of the initial, current and ultimate grain size distributions as functions of the grain size w and d_{min} and d_{Max} are the smallest and largest grain sizes present in any of the distributions. We assume that both the initial and ultimate GSDs are known (by mathematical definition or laboratory analysis in the case of the initial GSD, or by analysis of exhumed faults in the relevant rock type, in the case of the ultimate GSD). Here, we assume a probability density for the initial GSD p_0 given by

$$\hat{p}_0(w) = \delta(w - d_{Max}), \tag{2}$$

where δ is the Dirac delta function. We assume that the probability density for the ultimate GSD p_u follows a power law:

$$\hat{p}_u(w) = \frac{3-\alpha}{{d_{Max}}^{3-\alpha} - {d_{min}}^{3-\alpha}} w^{2-\alpha}, \tag{3}$$

where α is a dimensionless constant with typical values of $2.5 - 2.8$. Then, we are able to express the probability density of the current GSD by

$$\hat{p}(w, B) = \hat{p}_0(w)(1 - B) + \hat{p}_u(w)B, \tag{4}$$

We are also able to construct three grading constants given by

$$\theta_\gamma = 1 - \frac{3-\alpha}{5-\alpha}\left(\frac{1-(d_{min}/d_{Max})^{5-\alpha}}{1-(d_{min}/d_{Max})^{3-\alpha}}\right), \tag{5}$$

$$\theta_\kappa = 1 - \frac{3-\alpha}{7-\alpha}\left(\frac{1-(d_{min}/d_{Max})^{7-\alpha}}{1-(d_{min}/d_{Max})^{3-\alpha}}\right), \tag{6}$$

$$\theta_I = 1 - \frac{3-\alpha}{8-\alpha}\left(\frac{1-(d_{min}/d_{Max})^{8-\alpha}}{1-(d_{min}/d_{Max})^{3-\alpha}}\right). \tag{7}$$

Now, following the small strain assumption, using the Einstein summation convention, and denoting time derivatives with an overdot, we consider $\dot{u}_i$, our rate of translation along the x_i axes, and $\dot{\omega}^c_i$, the relative Cosserat micro-rotation about the x_i axes. Our strain rate and curvature rate tensors are then given by

$$\dot{\gamma}_{ij} = \dot{u}_{i,j} + \epsilon_{ijk}\dot{\omega}^c_k, \tag{8}$$

$$\dot{\kappa}_{ij} = \dot{\omega}^c_{i,j}, \tag{9}$$

where ϵ_{ijk} is the Levi–Civita symbol. Both strain and curvature rate tensors can be split into their trace and deviatoric parts:

$$\dot{\gamma}_{ij} = \frac{1}{3}\dot{\gamma}_{kk}\delta_{ij} + \dot{e}_{ij}, \tag{10}$$

$$\dot{\kappa}_{ij} = \frac{1}{3}\dot{\kappa}_{kk}\delta_{ij} + \dot{z}_{ij}, \tag{11}$$

where $\dot{\gamma}_{kk} = \dot{\varepsilon}_v$ the volumetric strain rate and δ_{ij} is the Kronecker delta. Finally, the strain and curvature rates (as well as their trace and deviatoric components) can be decomposed into their elastic and plastic parts:

$$\dot{\gamma}_{ij} = \dot{\gamma}^e_{ij} + \dot{\gamma}^p_{ij}, \tag{12}$$

$$\dot{\kappa}_{ij} = \dot{\kappa}^e_{ij} + \dot{\kappa}^p_{ij}. \tag{13}$$

We consider the mass density of the continuum material ρ, as well as the solid mass density ρ_s. From this, we may define the solid fraction as a state variable, given by

$$\phi = \frac{\rho}{\rho_s}. \tag{14}$$

For a given GSD determined by B, there exist minimum and maximum possible values for the solid fraction, which we define by [6]

$$\phi_{min} = 1 - \alpha_{lower}(1 - B)^{l_\phi}\exp(-l_\phi B), \tag{15}$$

$$\phi_{Max} = 1 - \alpha_{upper}(1 - B)^{u_\phi}\exp(-u_\phi B), \tag{16}$$

where α_{lower} and α_{upper} are terms giving the lower and upper solid fraction limits for $B = 0$ and l_ϕ and u_ϕ are index terms controlling the evolution of the limits with B. From these expressions, we define the relative solid fraction χ by

$$\chi = \frac{\phi - \phi_{min}}{\phi_{Max} - \phi_{min}}. \tag{17}$$

We define the (nonsymmetric) stress tensor τ_{ij} and the couple-stress tensor μ_{ij}, which are respectively dual in power to the strain rate and curvature rate tensors, and decompose them into their trace and deviatoric parts:

$$\tau_{ij} = \frac{1}{3}\tau_{kk}\delta_{ij} + s_{ij}, \tag{18}$$

$$\mu_{ij} = \frac{1}{3}\mu_{kk}\delta_{ij} + m_{ij}, \tag{19}$$

where the mean stress $p = \frac{1}{3}\tau_{kk}$. We define the second deviatoric stress invariant q by

$$q = \sqrt{\frac{6}{5}s_{ij}s_{ij} + \frac{3}{10}s_{ij}s_{ji} + \frac{1}{{\ell^e}^2}\left(\frac{6}{5}m_{ij}m_{ij} + \frac{3}{10}m_{ij}m_{ji}\right)}, \tag{20}$$

where ℓ^e is the internal length scale given by [4]

$$\ell^e = d_{Max}\sqrt{1-\theta_\kappa B}. \tag{21}$$

Finally, we also note the existence of the breakage energy E_B, which is the energetic dual of the breakage B.

2.2 Model

We present a slightly modified version of the model developed in [5], to which we refer the reader for the full development. The stress-like variables are derived from an energy potential in the standard manner and are given by

$$\begin{aligned}
\tau^e_{ij} &= \left(\frac{\rho}{\rho^\star_s}\right)^n (1-\theta_\gamma B) C^e_{ijkl}\gamma^e_{kl}, && (22)\\
\tau_{ij} &= \tau^e_{ij} + \left(\frac{\rho}{\rho^\star_s}\right)^n \frac{n-1}{2}\left[(1-\theta_\gamma B) C^e_{klmn}\gamma^e_{kl}\gamma^e_{mn}\right. && (23)\\
&\qquad \left. +(1-\theta_\kappa B) {d_{\mathrm{Max}}}^2 D^e_{klmn}\kappa^e_{kl}\kappa^e_{mn}\right]\delta_{ij},\\
\mu_{ij} &= \left(\frac{\rho}{\rho^\star_s}\right)^n (1-\theta_\kappa B) {d_{\mathrm{Max}}}^2 D^e_{ijkl}\kappa^e_{kl}, && (24)\\
E_B &= \left(\frac{\rho}{\rho^\star_s}\right)^n \left(\frac{\theta_\gamma}{2} C^e_{ijkl}\gamma^e_{ij}\gamma^e_{kl} + \frac{\theta_\kappa}{2}{d_{\mathrm{Max}}}^2 D^e_{ijkl}\kappa^e_{ij}\kappa^e_{kl}\right), && (25)
\end{aligned}$$

where $\rho^\star_s$ is the unstressed solid density and C^e_{ijkl} and D^e_{ijkl} are the elastic tensors given by

$$\begin{aligned}
C^e_{ijkl} &= \left(\bar{K} - \tfrac{2\bar{G}}{3}\right)\delta_{ij}\delta_{kl} + (\bar{G}+\bar{G}_c)\delta_{ik}\delta_{jl} + (\bar{G}-\bar{G}_c)\delta_{il}\delta_{jk}, && (26)\\
D^e_{ijkl} &= \left(\bar{L} - \tfrac{2\bar{H}}{3}\right)\delta_{ij}\delta_{kl} + (\bar{H}+\bar{H}_c)\delta_{ik}\delta_{jl} + (\bar{H}-\bar{H}_c)\delta_{il}\delta_{jk}, && (27)
\end{aligned}$$

where $\bar{K}$ and $\bar{G}$ are the nonlinear bulk and shear stiffnesses respectively, and $\bar{G}_c$, $\bar{L}$, $\bar{H}$ and $\bar{H}_c$ are Cosserat stiffnesses. τ^e_{ij} is the elastic (as distinct from total) stress and can be decomposed into trace (p^e) and deviatoric parts similarly.

We introduce a function F given by

$$F = \sqrt{\frac{E_B}{E_c}}(1-B) - \zeta\chi, \tag{28}$$

where E_c is the critical breakage energy associated with the start of grain crushing, and ζ is a parameter that controls the dilation of the material under shearing. Then, the yield function of the material is given by

$$y = F^2 + \left(\frac{q}{(1-B)^a\left(Mp^e + \phi c\right)}\right)^2 - 1 \leq 0, \tag{29}$$

where c is a parameter controlling the cohesion of the material, a is a parameter controlling the shear strength reduction with increasing breakage and M is a function given by

$$M = M_0(1 + \zeta\mathcal{H}(-F)F), \tag{30}$$

where $\mathcal{H}(x)$ is the Heaviside step function defined by $\mathcal{H}(x) = 0$ if $x < 0$ and $\mathcal{H}(x) = 1$ if $x \geq 0$. M_0 is a function defined by

$$M_0 = \frac{3\sin(\varphi)}{\sqrt{3}\cos(\beta) - \sin(\beta)\sin(\varphi)}, \tag{31}$$

where φ is the internal friction angle, and β is the Lode angle given in the Cosserat continuum by

$$\beta = \frac{1}{3}\arcsin\left(\frac{27}{2}\frac{\det(s_{ij})}{q^3}\right), \tag{32}$$

where the values lie between $-\pi/6$ and $\pi/6$, and triaxial compression has a Lode angle of $\pi/6$.

Finally, we must specify the evolution laws of the system, which we develop using the h^2-plasticity framework [7] are given by

$$\begin{aligned}
\dot{\rho} &= \rho\dot{\varepsilon}_v, && (33)\\
\dot{\phi} &= \dot{\phi}^e + \dot{\phi}^p, && (34)\\
\dot{\phi}^e &= \phi(1-\chi)\dot{\varepsilon}^e_v, && (35)\\
\dot{\phi}^p &= \langle\lambda\rangle(1-\langle -y\rangle)^s F\frac{2\phi(1-B)}{p^e}\sqrt{\frac{E_B}{E_c}}\sin^2(\omega), && (36)
\end{aligned}$$

Table 1: Material parameters taken from the literature

Parameter	Value	Unit	Source
d_{min}	0.001	mm	Kendall [8]
d_{Max}	0.25	mm	Ouffrouk [9]
α	2.6	—	An & Sammis [10]
α_{lower}	0.28	—	Bourbié & Zinszner [11]
α_{upper}	0.03	—	Bourbié & Zinszner [11]
u_ϕ	0.12	—	Cil et al. [6]
l_ϕ	0.16	—	Cil et al. [6]
n	3	—	Alaei et al. [12]
$\rho_s^\star$	2.65×10^{-3}	g/mm^3	Goodfellow et al. [13]

$$\dot{B} = \langle\lambda\rangle(1-\langle -y\rangle)^s\langle F\rangle\frac{R(1-B)}{\sqrt{E_B E_c}}\cos^2(\omega) \tag{37}$$

$$\dot{\gamma}_{ij}^p = \langle\lambda\rangle(1-\langle -y\rangle)^s\left[F\frac{2(1-B)}{p^e}\sqrt{\frac{E_B}{E_c}}\sin^2(\omega)\delta_{ij} + \frac{2}{[(1-B)^a(Mp^e+\phi c)]^2}\left(\frac{6}{5}s_{ij}^e+\frac{3}{10}s_{ji}^e\right)\right], \tag{38}$$

$$\dot{\kappa}_{ij}^p = \langle\lambda\rangle(1-\langle -y\rangle)^s\frac{2}{[(1-B)^a(Mp^e+\phi c)]^2}\left(\frac{6}{5}m_{ij}^e+\frac{3}{10}m_{ji}^e\right), \tag{39}$$

where R is a parameter controlling the rate of grain breakage, s is a parameter controlling the smoothness of the constitutive response, the Macaulay brackets give $\langle x\rangle = (x+|x|)/2$, λ is the plastic multiplier and ω is a coupling angle given by

$$\omega = \frac{\pi}{2}\left[1-\chi\mathcal{H}(F)\right]. \tag{40}$$

The model is integrated numerically using a standard implicit Euler time discretisation and a classical return-mapping algorithm that determines the value of λ along with the state variables. By taking the time derivatives of the stresses and couple-stresses and rearranging in terms of the strain and curvature rates, we obtain the incremental elastoplastic stiffness tensors E_{ijkl}^{ep} and F_{ijkl}^{ep} (linking the stress rate with the strain and curvature rates respectively) and K_{ijkl}^{ep} and M_{ijkl}^{ep} (linking the couple-stress rate with the strain and curvature rates respectively).

2.3 Linear stability analysis

In order to determine the width and orientation of shear bands, we conduct a linear stability analysis by perturbing the underlying displacement and micro-rotation fields and studying the effects on the equilibrium equations of the Cosserat continuum:

$$\tau_{ij,j} - \rho\ddot{u}_i = 0_i, \tag{41}$$

$$\mu_{ij,j} - \epsilon_{ijk}\tau_{jk} - I\ddot{\omega}_i^c = 0_i, \tag{42}$$

where I is the moment of microrotational inertia (given by $I = (\pi/60)\rho(1-\theta_I B){d_{Max}}^5$ [4]), assuming that the perturbations follow the incremental stress and couple-stress rate relationships, then assuming the perturbations have solutions of the form

$$U_i^\star(x_j,t) = \bar{U}_i e^{st+\frac{2\pi \mathrm{i}}{\Lambda}x_j n_j}, \tag{43}$$

$$\Omega_i^\star(x_j,t) = \bar{\Omega}_i e^{st+\frac{2\pi \mathrm{i}}{\Lambda}x_j n_j}, \tag{44}$$

where $\bar{U}_i$ and $\bar{\Omega}_i$ are constants, s is the Lyapunov growth coefficient, Λ is the perturbation wavelength and n_j is the polarisation vector of the perturbation. For a given set of state variables and after having converted from the Cartesian to cylindrical coordinate systems, we write the matrix acting on the $\bar{U}_i$ and $\bar{\Omega}_i$ and analyse whether that matrix becomes singular by finding the roots of its characteristic polynomial written in terms of s. In particular, we search for the n_i and Λ associated with the root of the polynomial that has the largest positive real part (if such a root exists), which is the perturbation that grows the fastest. The shear band that is the physical realisation of this perturbation has a resulting thickness $\Lambda/2$ and orientation n_j.

3 Calibration

The model parameters are calibrated using values directly from the literature on Fontainebleau sandstone, or following more general arguments about granular rocks. These values are listed in Table 1.

Table 2: Material parameters obtained from fitting against the elastic parameters reported by Ouffroukh [9]

Parameter	Value (MPa)
K	39487
$\bar{G}$	31332
$\bar{G}_c$	52220
$\bar{L}$	0
$\bar{H}$	31332
$\bar{H}_c$	52220

Table 3: Material parameters obtained from fitting against the peak stresses reported by Ouffroukh [9]

Parameter	Value	Unit
E_c	4.0	MPa
φ	0.9	—
c	24.1	MPa
s	20	—

We have three parameters that are free to specify, namely ζ, a and R, which we set to 0.5, 3 and 8 respectively. Using data from Ouffroukh [9], we calibrate the nonlinear bulk and shear stiffnesses by setting $B = 0$, obtaining the material density using the reported porosity value of 21%, taking an average of the reported Poisson's ratio ν for the first cycle of the cyclic drained triaxial compression tests, then calculating the value of $\bar{G}$ that minimises the least squares difference with the reported shear modulus at each confining stress. $\bar{K}$ is then calculated using the standard linear elastic relationship between K, G and ν (as the nonlinear scaling by the density acts equally on $\bar{K}$ and $\bar{G}$, the classical relation still holds). Now, using the calibration method given in [4], we obtain directly the Cosserat stiffnesses by $\bar{G}_c = 5\bar{G}/3$, $\bar{L} = 0$, $\bar{H} = \bar{G}$ and $\bar{H}_c = 5\bar{G}/3$. The obtained values are listed in Table 2.

Finally, there remains four parameters to calibrate, namely E_c, φ, c and s. We vary these against the axial-strain and differential-stress data provided by Ouffroukh [9] to obtain the calibrated values reported in Table 3.

4 Results

We compare the predictions of the calibrated model against data obtained from two drained triaxial compaction experiments reported by Ouffroukh, one at 40 MPa confining pressure and the other at 50 MPa, both compacted to 1% axial strain. The comparison with the experimental axial strain and deviatoric stress results are shown in Figure 1.

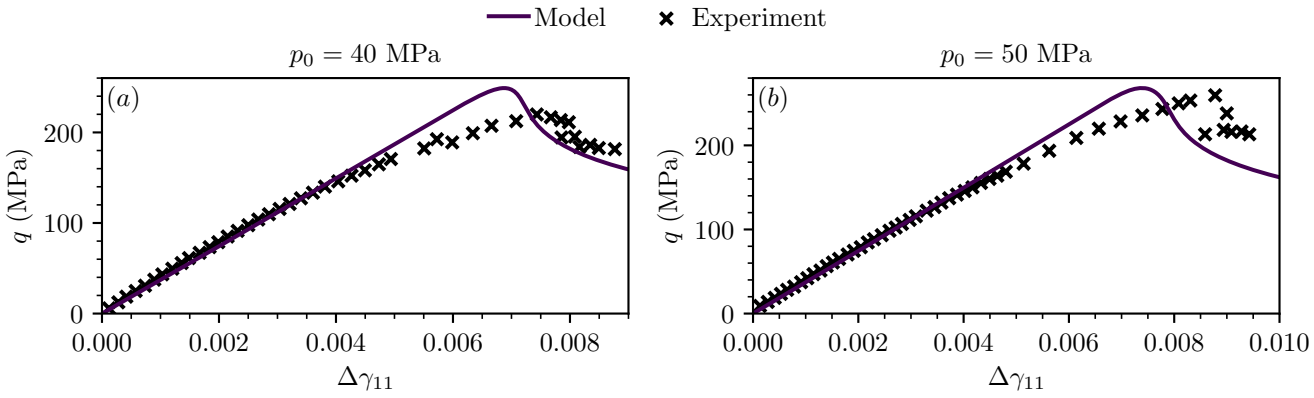

Figure 1: The predictions of the model against the experimental data reported by Ouffroukh [9].

We see that the model captures very well the initial elastic loading of the system, and also accurately models the stress drops that occur immediately after obtaining the peak stress. While some part of the stress relaxation prior to the stress drop is not captured by the model, the h^2-plasticity does enable the model to relax the stresses relative to what they would be in a pure elasto-plastic model. However, it is also noticeable that the stress peak and drop occur after slightly more straining than predicted by the model. Nevertheless, we consider that the model successfully captures the important features of the stress-strain response of the material.

In Figure 2, we consider the evolution of the B and ϕ internal variables of the system.

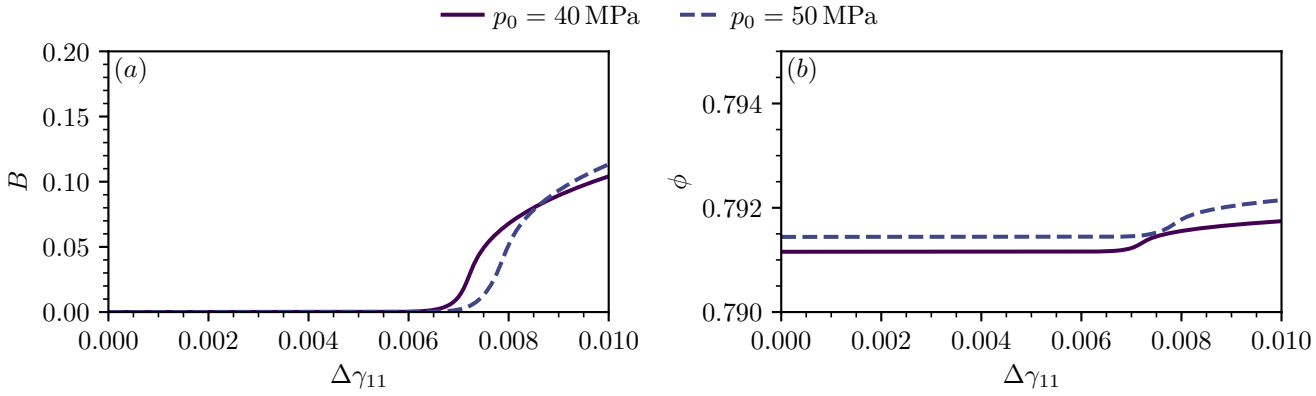

Figure 2: The evolutions of the internal breakage B and solid fraction ϕ variables for the simulations corresponding to initial confining pressure of 40 and 50 MPa.

We observe that the evolution of the grain breakage is rapid in both simulations, with the 50 MPa confining pressure developing more grain breakage, albeit starting slightly later in the simulation. By contrast, the solid fraction only evolves slightly, with the breakage taking the dominant role in energy dissipation. We may compare this with the shear band shown in Figure 3, in which we observe very substantial grain breakage and a pore space that is diffused over many more individual pores, rather than in large distinct pores. We thus conclude that the model is accurately capturing the microstructural evolution of the experimental samples.

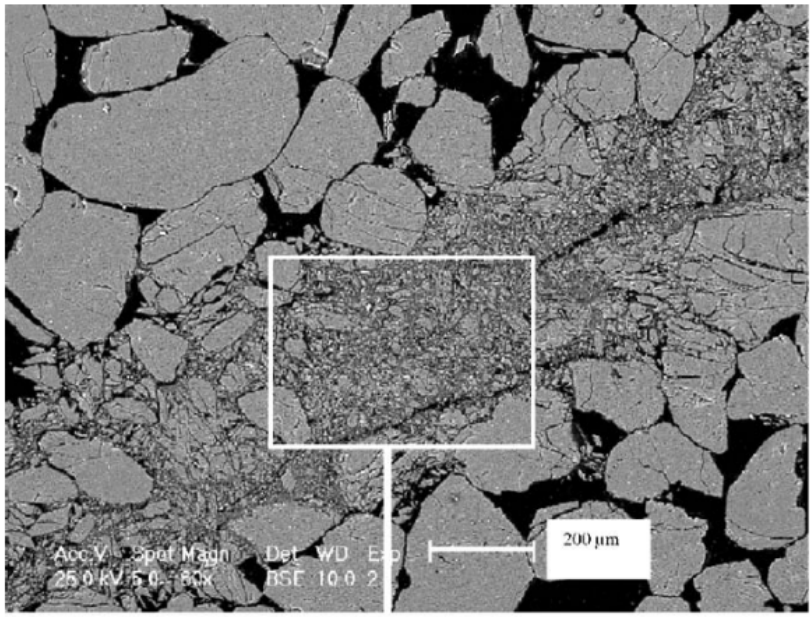

Figure 3: A microphotograph of a shear band formed in a drained test of Fontainebleau sandstone confined at 50 MPa, taken from [14].

Finally, after conducting linear stability analyses where we set the radius to conduct the analysis at to 18.75 mm to match the size of the experimental samples, we obtain predicted shear band widths of 1.94 mm and 1.55 mm for the 40 and 50 MPa confining stress systems respectively. These are slightly thicker than the range of 0.2–1 mm reported by Ouffroukh for these systems. The orientations of the bands are at 49.9° and 48.2° to the horizontal for the two systems, which is slightly less inclined than the observed values, which are in the range of 54–60°.

5 Conclusions

We have presented a model that accounts for grain breakage and the reduction of pore space in a micro-physically motivated fashion, using only variables that are experimentally accessible and well-established in the literature. The model has been calibrated from data available in the literature, and comparisons of model predictions against historical experiments demonstrates that the important features of the stress-strain behaviour are accurately captured. A comparison of the predicted localization behaviour with historical results demonstrated that the model can predict the shear band thickness and orientation with good accuracy. The results demonstrate that the breakage mechanics framework, suitably enriched with the Cosserat continuum, is able to predict the behaviour of porous granular rocks such as Fontainebleau sandstones in terms of both material behaviour and the emergence of structural features such as shear bands.

Acknowledgements

The third author acknowledges the European Research Council's (ERC) support under the European Union's Horizon 2020 research and innovation programme (Grant agreement ID 101087771 INJECT). Views and opinions expressed are however those of the authors only and do not necessarily reflect those of the European Union or Horizon Europe. Neither the European Union nor the granting authority can be held responsible for them.

Declaration of competing interests

The authors have no competing interests to declare that are relevant to the content of this article.

References

[1] Vardoulakis, I., Sulem, J.: Bifurcation Analysis in Geomechanics. 1st edn. Blackie Academic & Professional, Glasgow, 1995.

[2] Einav, I.: Breakage mechanics — Part I: Theory. Journal of the Mechanics and Physics of Solids **55**(6), 1274–1297 (2007)

[3] Einav, I.: Breakage mechanics — Part II: Modelling granular materials. Journal of the Mechanics and Physics of Solids **55**(6), 1298–1320 (2007)

[4] Collins-Craft, N.A., Stefanou, I., Sulem, J., Einav, I.: A Cosserat Breakage Mechanics model for brittle granular media. Journal of the Mechanics and Physics of Solids **141**, 103975 (2020)

[5] Collins-Craft, N.A., Stefanou, I., Sulem, J., Einav, I.: The Influence of Grain Crushing and Pore Collapse on the Formation of Faults. Journal of Geophysical Research: Solid Earth **131**(3), e2025JB033062 (2026)

[6] Cil, M.B., Hurley, R.C., Graham-Brady, L.: Constitutive Model for Brittle Granular Materials Considering Competition between Breakage and Dilation. Journal of Engineering Mechanics **146**(1), 1–12 (2020)

[7] Einav, I.: The unification of hypo-plastic and elasto-plastic theories. International Journal of Solids and Structures **49**(11–12), 1305–1315 (2012)

[8] Kendall, K.: The impossibility of comminuting small particles by compression. Nature **272**(4), 710–711 (1978)

[9] Ouffroukh, H.: Comportement hydromécanique d'une roche granulaire et localization des déformations. PhD thesis, École nationale des ponts et chaussées, 2004.

[10] An, L.-J., Sammis, C.G.: Particle Size Distribution of Cataclastic Fault Materials from Southern California: A 3-D Study. Pure and applied geophysics **143**(1–3), 203–227 (1994)

[11] Bourbié, T., Zinszner, B.: Hydraulic and Acoustic Properties as a Function of Porosity in Fontainebleau Sandstone. Journal of Geophysical Research: Solid Earth **90**(B13), 11524–11532 (1985)

[12] Alaei, E., Marks, B., Einav, I.: A five-parameter hydrodynamic-plastic model for crushable sand. International Journal of Solids and Structures **254–255**, 111914 (2022)

[13] Goodfellow, S.D., Tisato, N., Ghofranitabari, M., Nasseri, M.H.B., Young, R.P.: Attenuation Properties of Fontainebleau Sandstone During True-Triaxial Deformation Using Active and Passive Ultrasonics. Rock Mechanics and Rock Engineering **48**(6), 2551–2566 (2015)

[14] Sulem, J., Ouffroukh, H.: Shear banding in drained and undrained triaxial tests on a saturated sandstone: Porosity and permeability evolution. International Journal of Rock Mechanics and Mining Sciences **43**(2), 292–310 (2006)